

Multi-modal Aggregation Network for Fast MR Imaging

Chun-Mei Feng, Huazhu Fu, Tianfei Zhou, Yong Xu, *Member, IEEE*,
 Ling Shao, *Fellow, IEEE*, David Zhang, *Life Fellow, IEEE*,

Abstract—Magnetic resonance (MR) imaging is a commonly used scanning technique for disease detection, diagnosis and treatment monitoring. Although it is able to produce detailed images of organs and tissues with better contrast, it suffers from a long acquisition time, which makes the image quality vulnerable to say motion artifacts. Recently, many approaches have been developed to reconstruct full-sampled images from partially observed measurements in order to accelerate MR imaging. However, most of these efforts focus on reconstruction over a single modality or simple fusion of multiple modalities, neglecting the discovery of correlation knowledge at different feature level. In this work, we propose a novel Multi-modal Aggregation Network, named MANet, which is capable of discovering complementary representations from a fully sampled auxiliary modality, with which to hierarchically guide the reconstruction of a given target modality. In our MANet, the representations from the fully sampled auxiliary and undersampled target modalities are learned independently through a specific network. Then, a guided attention module is introduced in each convolutional stage to selectively aggregate multi-modal features for better reconstruction, yielding comprehensive, multi-scale, multi-modal feature fusion. Moreover, our MANet follows a hybrid domain learning framework, which allows it to simultaneously recover the frequency signal in the k -space domain as well as restore the image details from the image domain. Extensive experiments demonstrate the superiority of the proposed approach over state-of-the-art MR image reconstruction methods.

Index Terms—MR imaging, multi-modal fusion, image reconstruction.

I. INTRODUCTION

MAGNETIC Magnetic resonance (MR) imaging is a widespread scanning technique for musculoskeletal, neurological, and oncological diseases [1]. The raw data obtained by the scanner complex-valued data, collected in k -space and transferred to the image domain by inverse 2D

C.-M. Feng and Y. Xu are with the Shenzhen Key Laboratory of Visual Object Detection and Recognition, Harbin Institute of Technology (Shenzhen), 518055, China. (Email: strawberry.feng0304@gmail.com; yongxu@ymail.com). (Corresponding author: Huazhu Fu, Yong Xu)

H. Fu is with the Institute of High Performance Computing (IHPC), Agency for Science, Technology and Research (A*STAR), Singapore 138632. (Email: hzfu@ieee.org)

L. Shao are with the Inception Institute of Artificial Intelligence, Abu Dhabi, UAE. (Email: ling.shao@ieee.org).

T. Zhou is with ETH Zurich, Switzerland. (Email: tianfei.zhou@vision.ee.ethz.ch)

D. Zhang is with the School of Science and Engineering, The Chinese University of Hong Kong (Shenzhen), Shenzhen 518172, China, also with the Shenzhen Research Institute of Big Data, Shenzhen 518172, China, and also with the Shenzhen Institute of Artificial Intelligence and Robotics for Society, Shenzhen 518172, China (Email: davidzhang@cuhk.edu.cn)

This work was done during the internship of Chun-Mei Feng at Inception Institute of Artificial Intelligence.

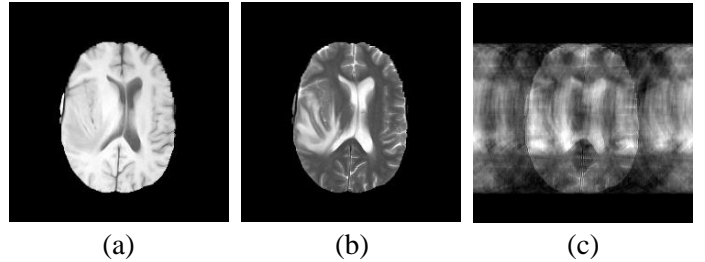


Fig. 1: Exemplars of two different modalities. (a) The fully-sampled T1 MR image. (b) The fully-sampled T2 weighted MR image. (c) The undersampled T2 weight image under a 1D random sampling mask with 3 \times acceleration. Given (c) as an input, this work aims to achieve high-fidelity reconstruction (b) by incorporating the prior knowledge from (a).

Fourier transform [2]. However, the physical nature of the MR data acquisition process makes the scanning time up to tens of minutes long, causing uncomfortable examination experiences and high health care costs [3]. Therefore, accelerated MR image reconstruction is a major ongoing research goal towards improving the patient experience.

Reconstructing images from undersampled k -space measurements is a standard method to accelerate MR imaging. However, obtained a basic reconstruction of zero-filled k -space data often exhibit aliasing artifacts (shown in Fig. 1 (c)), making them inappropriate for clinical diagnosis [2, 4]. Therefore, how to reduce these artifacts and recover high-fidelity images from the insufficient k -space measurements becomes the goal of MR image reconstruction systems. Relying on the inherently redundant in k -space [5], compressed sensing (CS) and parallel imaging have made significant progress in MR image reconstruction [6, 7, 8, 9, 10, 11]. CS-based methods can accelerate the acquisition of MR images by taking fewer samples than traditional signal processing methods. Further, by incorporating additional prior knowledge of the image, CS can solve the aliasing artifacts by violating the Shannon-Nyquist sampling theorem [12]. However, CS-based methods for MR image reconstruction require significant time for iterative minimization, resulting in difficulty in near-real-time MR image scenarios, *e.g.*, cardio-MR and functional-MR imaging [13]. Parallel imaging reconstructs the images from multi-channel aliased images using the coil sensitivity profiles through multiple-channels, but it will cause artifacts if the in-plane acceleration rate is higher than 2 [14].

Recently, deep learning techniques have been widely used

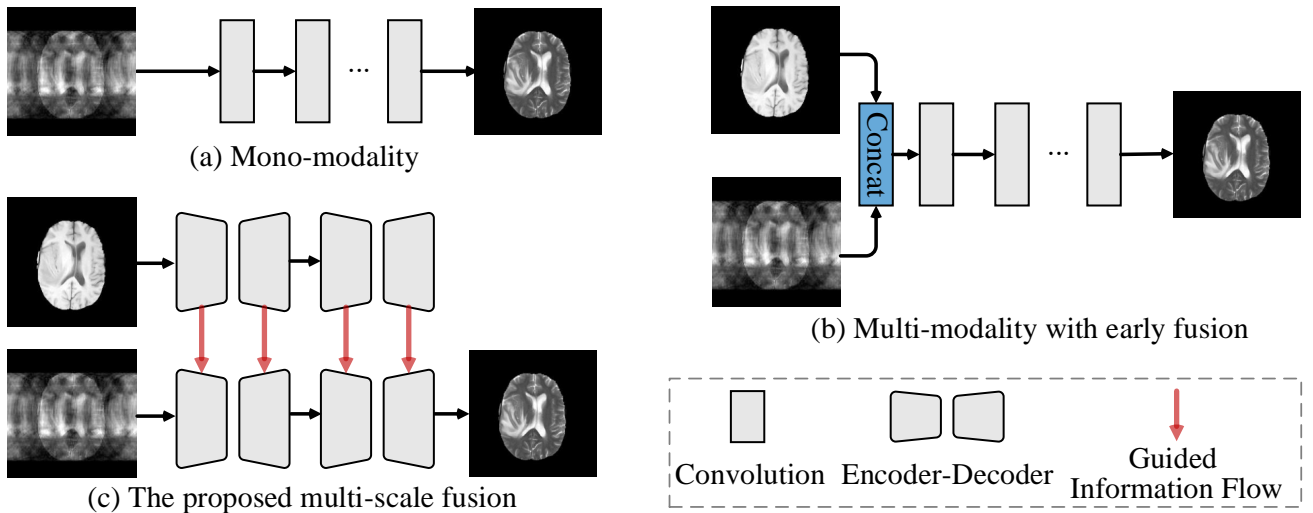


Fig. 2: Typical MR reconstruction schemes. (a) Reconstruction using a single modality; (b) Images in two modalities are concatenated together first as the input; (c) Our model conducts the multi-scale fusion of multiple modalities to learn comprehensive feature representations.

for MR image reconstruction [3, 8, 15, 16, 17, 18, 19, 20]. However, most of these methods focus on using undersampled data of a mono-modal acquisition to reconstruct high-quality MR images (shown in Fig. 2(a)). Thus, using MR sequences with shorter acquisition times to assist the collection of other sequences with closely related structural information is a new idea to accelerate MR imaging [21]. For example, T1 and T2 weighted images are two closely related MR sequences, but T2 weighted imaging is slower than T1 weighted due to its relatively longer TRs and TEs. Therefore, we can use the T1 weight as complementary modality to guide T2 weighted image reconstruction. Specifically, Fig. 1 shows two different-modality MR sequences from the same subject. Image (a) is the T1 weighted image, which is used to identify fatty tissue, obtain morphological information, and for post-contrast imaging; (b) is the T2 weighted image, which is used to detect edema, inflammation and assess anatomical structure. Only a few studies have attempted to conduct multi-modal fusion between different MR sequences to accelerate image reconstruction [21], *e.g.*, reconstruct the high-quality T2 weighted image according to the high coupling relationship between T1 and T2 images [21, 22]. However, [21] directly integrates T1 and T2 images as a two-channel input, using early fusion (shown in Fig. 2 (b)). Similarly, [22] directly adds T1 to the input of each block as the prior information to recover images. Though impressive, existing methods stacking T1 image and T2 image directly into the network do not explore the feature level information, which are especially critical for T2 weighted image reconstruction.

To explore the hierarchical correlations between different modalities, we take a further step and fuse the target modality image (*e.g.*, T2) with another one (*e.g.*, T1 weighted) in a multi-scale manner (shown in Fig. 2(c)). Specifically, we propose a Multi-modal Aggregation Network, named MANet, to learn the fusion of multi-modality features in different scales. Unlike previous methods that only take T1 weights as priors,

our MANet enhances the learning of the T1 stream at multiple scales with T1-guided attention modules. Specifically, we design a two-stream network to learn a specific representation for each modality. The attention module fuses the T1 weighted features in each convolutional stage to learn effective feature representations. It then enhances the T1 features to guide the learning of T2 features. Finally, benefiting from these modality-specific networks and fusion module, our MANet can learn a latent representation in a complementary way to generate the target images. The superiority of the proposed fusion method is validated by various experiments.

The contributions of this paper are four-fold: **(1)** Different from the existing multi-modality fusion methods, we propose a new multi-modality aggregation MR image reconstruction framework, which can excavate the multi-scale features of auxiliary modality for target modality reconstruction. The proposed method considers the complementary and diversity of different MR modalities. **(2)** A hybrid domain learning scheme is designed to incorporate the k -space information of the frequency domain, which can compensate for the structural and non-local loss of MR image reconstruction in the image-only domain. **(3)** Rather than concatenating the multi-modality features directly, a novel T1-guided attention module is proposed to enhance the features from the T1 weight, which provides a robust fusion method to identify the latent features specific to the target modality and effectively boosts the fusion performance. **(4)** Extensive experiments demonstrate that our proposed method generates superior MR reconstructions and achieves state-of-the-art performance. We show that incorporating T1 prior information is an effective solution for improving T2 MR reconstruction, especially for feature-level aggregation. The code is available at <https://github.com/chunmeifeng/MANet>.

II. RELATED WORKS

A. Deep Learning for MR Image Reconstruction

To accelerate the acquisition of MR images, a vast number of studies are devoted to dealing with the problem of undersampled MR image reconstruction. Signal processing techniques, such as CS and low-rank machine learning methods have achieved significant progresses in fast MR imaging [8, 9, 11, 23, 24, 25, 26, 27, 28]. Since most of the information in an image can be expressed by a linear combination of sparse signals [29], previous works have mainly focused on combining the sparse coefficients of a sparse transform, such as the wavelet transform [30, 31, 32], dictionary learning [33, 34] or the contourlet transform [35], with regularization parameters to solve the inverse problem. However, these tends to lead to more artifacts and the loss of details in the reconstruction, because the high undersampling rate will result in smaller sparse coefficient values. More importantly, these iterative algorithms are often overly smooth and time consuming, limiting their practical scalability, *e.g.*, to real-time MR image scenarios.

To overcome these limitations, deep learning based methods have been applied to MR image reconstruction [3, 18, 22]. These can fully exploit the inherent properties of the images based on a large amount of training data, instead of relying on prior information as traditional imaging techniques. We can divide deep learning based methods into two groups: model-based unrolling [8, 25, 36, 37] and end-to-end learning methods. For model-based unrolling methods, a typical example is ADMM-Net [8, 38], which uses the alternated direction method of multipliers (ADMM) algorithm to optimize the unrolled deep architecture. Chen *et al.* then extended ADMM-Net to multi-coil MR images for parallel imaging [25]. MoDL takes deep learning as a prior and benefits from the advantages of data-driven learning to achieve good results in MR image reconstruction [37]. For end-to-end learning methods, Wang *et al.* [15] were the first to propose a Convolutional Neural Network (CNN) to learn the mapping from an undersampled MR image to a reconstructed image. UNet was used to solve the inverse problem and capture spatial information [39, 40]. Zhu *et al.* proposed an automated transform by manifold approximation (AUTOMAP) method to estimate the mapping between the sensor and image domain in the training data [41]. Using a network pre-trained on X-ray computed tomography (CT) and MR image datasets, Han *et al.* [42] proposed a deep network which can be fine-tuned with only a few MR images. By separately training the magnitude and phase networks using a residual learning network, Dongwook *et al.* [43] achieved a significant acceleration in MR reconstruction.

Following recent studies on natural image synthesis, GAN-based methods that use a generator and discriminator with a loss function have also been used for MR image reconstruction [16, 17, 44]. In addition to learning from specific network structures [44, 45, 46], image refinement mechanisms with different training objectives, *e.g.*, adversarial loss [16] and perceptual loss [17], are also gaining more attention. Wang *et al.* [47] and KIKI-Net [48] used hybrid domain learning schemes to incorporate k -space information along with image

domain information. However, their learning schemes are only applied to a single modality rather than the fusion of multiple modalities, and KIKI-Net is a deeply cascaded network. Our method not only learns the characteristics of the two modalities in the hybrid domain, but also designs a fusion mechanism that can combine the features of the two modalities in the hybrid domain.

B. Multi-Modal Feature Representation Learning

Multi-modal fusion has demonstrated effectiveness in a variety of computer vision tasks, *e.g.*, object tracking [49] image classification [50], and semantic segmentation [51, 52]. Many natural applications can be well learned by multi-modal fusion because of the multi-modal properties of the data. Since multi-modal learning employs the complementarity between multi-modal data, fusing various modalities has attracted increased attention recently. The advantage of multi-modality fusion is that, by learning to combine multiple modalities in a new space, it is more robust than using input features from any single modality [53]. For example, Soheil *et al.* [54] combined a sparsity constraint with a dictionary to learn multi-modal tasks. With the renaissance of deep learning, multi-modal fusion has shown significant effectiveness in various neural networks. For example, Nam *et al.* [55] proposed a dual attention network (DAN), which combines images and words to gather basic information. Huang *et al.* [56] proposed a multi-modal unsupervised image-to-image translation (MUNIT) framework to generate diverse outputs from a given source domain image. Based on a three-dimensional deep convolutional neural network, Nie *et al.* [57] fused T1 MR, functional (fMR imaging) and diffusion tensor imaging (DTI) data to predict the survival time of brain glioma patients. Fan *et al.* [58] applied multi-modal learning to recurrent neural networks for RGB-D scene labeling. To improve the reliability and accuracy of the system, Zhang *et al.* [49] designed a generic sensor-agnostic multi-modal MOT framework (mmMOT) for multi-object tracking. For medical images, several multi-modal fusion methods have been designed for image synthesis. For example, Zhou *et al.* [59] proposed a hybrid-fusion framework to learn a mapping between multi-modal source images and target images for multi-modality MR image synthesis. Michal *et al.* [60] presented a network with cascaded stages, which exploits multiple magnetic-resonance modalities for brain tumor segmentation. Instead of using traditional paired data as input for segmentation, Dou *et al.* [61] proposed an unpaired multi-modal image segmentation framework. Multi-modal representation has also been used for jointing MR and PET reconstruction simultaneously [62, 63]. Following [21], we build our model from the new perspective which use the MR sequences with shorter acquisition times to assist the collection of other sequences with closely related structural information to accelerate MR imaging.

C. Neural Attention Mechanisms

Attention mechanisms allows network to selectively pay attention to a subset of inputs, making the network intentionally focus on useful information to improve performance.

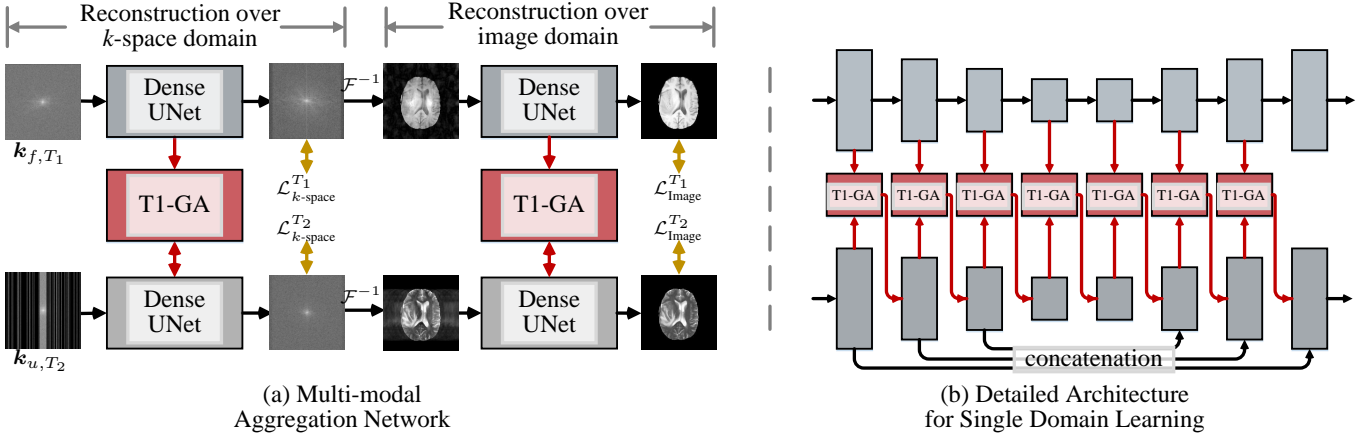


Fig. 3: (a) Illustration of the proposed multi-modality hybrid domain learning framework. (b) The detailed network architecture for learning in an individual domain.

Therefore, attention mechanisms have been widely explored in visual tasks, *e.g.*, scene segmentation [64, 65], image enhancement [66], tracking [67] and classification [68]. For example, Hu *et al.* [69] designed an attention-and-gating mechanism by learning the interdependence of channels. Zhang *et al.* [70] created a non-local attention mechanism to expand the receptive field, which enhances a network's ability to handle large-scale variation. Yu *et al.* [65] presented a smooth network to combine the channel attention block with global average pooling to select more discriminative features. Lu *et al.* [71] proposed a dual mechanism which jointly applies an image and question attention to highlight the image regions relevant to answering the question.

More recently, attention mechanisms have been studied in medical images [72, 73, 74, 75, 76]. In this way, the learned model can selectively focus on important image regions, such as the lesions in the segmentation task. For example, Sun *et al.* [77] used an attention-guided dense-upsampling network to segment whole breast mass mammograms. Inspired by the success of attention mechanisms in visual tasks, our attention module is used to selectively enhance the features of auxiliary modality, which are crucial to target images.

In this work, we introduce a deep multi-modal fusion method for accelerated MR image reconstruction, which helps to effectively explore the correlations between multi-modal images. Based on this, we design a multi-modal aggregation network for multi-scale fusion, which deeply fuses the two weighted images at multiple scales, yielding high-fidelity reconstructions.

III. PRELIMINARIES

Let \mathbf{x}_f represent the fully sampled image. We aim to reconstruct a fully sampled image \mathbf{x}'_f from undersampled k -space \mathbf{k}_u or undersampled image \mathbf{x}_u . The relationship between \mathbf{x}_u and \mathbf{k}_u is as follows:

$$\mathbf{x}_u = \mathcal{F}^{-1}(\mathbf{k}_u) + \epsilon = \mathcal{F}^{-1}(M \odot \mathcal{F}(\mathbf{x}_f)) + \epsilon, \quad (1)$$

where \mathcal{F} and \mathcal{F}^{-1} represent the 2D Fast Fourier Transform (FFT) and inverse FFT, M represents a binary mask operator

to select a subset of the k -space points, ϵ is the noise and \odot is the element-wise multiplication operation. It is worth noting that MR images obtained by \mathcal{F}^{-1} are complex-valued matrices. We can reconstruct \mathbf{x}'_f with prior knowledge of its properties, which can be formulated as the following optimization problem:

$$\mathbf{x}'_f = \arg \min_{\mathbf{x}_f} \|M \odot \mathcal{F}(\mathbf{x}_f) - \mathbf{k}_u\|_2^2 + \sum_i \lambda_i \psi_i(\mathbf{x}_f), \quad (2)$$

where ψ is a regularization function and λ_i is a weight controlling the trade-off between the regularization terms and data fidelity.

The ill-posed inverse problem in Eq. (2) of reconstructing \mathbf{x}'_f from limited sampled data can be effectively resolved by CNNs. Formally, Eq. (2) can be well approximated using neural networks by minimizing the following loss function:

$$\mathcal{L} = \frac{1}{N} \sum_{n=1}^N \mathcal{L}_{\text{Image}}(\mathcal{G}_\theta(\mathbf{x}_u^n), \mathbf{x}_f^n). \quad (3)$$

Here, given N training samples $\{\mathbf{x}_u^n, \mathbf{x}_f^n\}_{n=1}^N$, a neural network \mathcal{G}_θ , parameterized by θ , is learnt to reconstruct \mathbf{x}_f from \mathbf{x}_u . $\mathcal{L}_{\text{Image}}$ denotes the loss function for measuring the image-level reconstruction, for which a variety of losses (*e.g.*, l_1 , l_2 or SSIM losses) can be used.

IV. METHODOLOGY

This section presents the details of the proposed cascade multi-modal feature aggregation framework. We first explain our objective function in §IV-A. Then, in §IV-B, we provide detailed information of our network architecture. Last, we describe the T1-guided attention module for feature fusion in §IV-C.

A. Problem Definition

Rather than conducting reconstruction within a single modality, like in Eq. (3), our motivation is to learn correlation knowledge between two closely related modalities, and employ the knowledge to improve the reconstruction. In particular,

we use T1 weighted images as guidance for more accurate reconstruction of T2 weighted images. Thus, Eq. (3) becomes:

$$\mathcal{L} = \frac{1}{N} \sum_{n=1}^N \mathcal{L}_{\text{Image}}(\mathcal{G}_\theta(\mathbf{x}_{u,T_2}^n, \mathbf{x}_{f,T_1}^n), \mathbf{x}_{f,T_2}^n), \quad (4)$$

where \mathbf{x}_{f,T_2} is the fully-sampled T2 weighted image, \mathbf{x}_{u,T_2} is the undersampled T2 weighted image, and \mathbf{x}_{f,T_1} is the fully-sampled T1 weighted image. It is important to note that the T1 weighted images are mined as multi-scale features and fused into our framework. We aim to obtain a series of well-trained weights which are guided by the features of fully-sampled T1 weighted images.

B. Hybrid Domain Learning Framework

Our MANet adopts a hybrid domain learning framework to learn comprehensive feature representations from data in both k -space and image domains. As illustrated in Fig. 3 (a), the framework consists of two sequential stages. The first stage recovers signals from the undersampled k -space measurements and its outputs are transformed into the image domain for the second-stage image-aware reconstruction. In each stage, the corresponding T1 signal is employed to guide the reconstruction procedure.

More specifically, instead of only considering image-domain optimization as in Eq. (4), the framework optimizes a dual-domain (*i.e.*, k -space and image domain) learning objective, as follows:

$$\begin{aligned} \mathcal{L} = & \frac{1}{N} \sum_{n=1}^N (\mathcal{L}_{k\text{-space}}(\mathcal{G}_k(\mathbf{k}_{u,T_2}^n, \mathbf{k}_{f,T_1}^n), \mathbf{k}_{f,T_2}^n) \\ & + \mathcal{L}_{\text{Image}}(\mathcal{G}_\theta(\mathbf{x}_{u,T_2}^n, \mathbf{x}_{f,T_1}^n), \mathbf{x}_{f,T_2}^n)), \end{aligned} \quad (5)$$

where \mathcal{G}_k denotes the neural network for k -space reconstruction, and $\mathcal{L}_{k\text{-space}}$ is the corresponding loss function for measuring the results. In our network implementation, Eq. (5) is solved in the following manner (see Fig. 3 (a)):

$$\begin{aligned} \mathcal{L} = & \frac{1}{N} \sum_{n=1}^N \alpha \left((1-\beta) \mathcal{L}_{k\text{-space}}^{T_1} + \beta \mathcal{L}_{\text{Image}}^{T_1} \right) \\ & + (1-\alpha) \left((1-\beta) \mathcal{L}_{k\text{-space}}^{T_2} + \beta \mathcal{L}_{\text{Image}}^{T_2} \right), \end{aligned} \quad (6)$$

where $\mathcal{L}_{k\text{-space}}^{T_2}$ and $\mathcal{L}_{\text{Image}}^{T_2}$ denote the loss functions for the target T2 modality in the k -space and image domains, respectively. They are similar to $\mathcal{L}_{k\text{-space}}^{T_1}$ and $\mathcal{L}_{\text{Image}}^{T_1}$. α weight the trade-off between the image domain and k -space domain, and β weight the trade-off between the reconstruction of the two modalities. We apply a loss on the T1 weight to enable clear structural information to be preserved, and to guide the reconstruction of the target modality. The α s balance the weights of these losses. Eqs. (5-6) finally provide our MANet a multi-domain, multi-modal learning mechanism for reconstruction.

Our MANet takes the same network structure for learning in both the k -space and image domains. Specifically, two DenseUNets are employed for feature extraction for the T1 and T2 inputs, while a T1-guided attention module (T1-GA) is incorporated into each convolutional stage for guided learning,

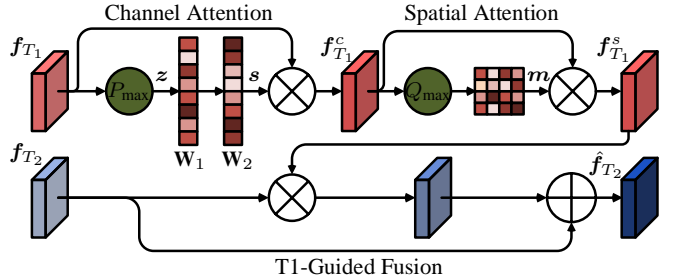


Fig. 4: Architecture of the T1-guided attention module (T1-GA) for multi-modal feature fusion.

as shown in Fig. 3 (b). In the following, we describe the details of the T1-guided attention module for multi-modal aggregation.

C. T1-Guided Attention Module

To ensure that the T1 weighted features can effectively guide the T2 weighted image reconstruction, we must fuse these two different modalities. Besides, any or redundancy and information that is not essential to both modalities must be reduced. Inspired by [78], we design a T1-guided attention module to improve the compatibility of the two different modalities and excavate fused features for T2 weighted image reconstruction. The detailed architecture of the module is depicted in Fig. 4.

In particular, we devise a novel T1-guided attention module \mathcal{H} to enrich the T2 weighted features. We denote $\mathbf{f}_{T_1} \in \mathbb{R}^{H \times W \times C}$ and $\mathbf{f}_{T_2} \in \mathbb{R}^{H \times W \times C}$ as the convolutional features of the T1 and T2 weighted images, respectively. The attention module can be formulated as:

$$\hat{\mathbf{f}}_{T_2} = \mathcal{H}(\mathbf{f}_{T_1}, \mathbf{f}_{T_2}) \in \mathbb{R}^{H \times W \times C}, \quad (7)$$

where $\hat{\mathbf{f}}_{T_2}$ indicates the enhanced feature of the T2 modality, which is used as the input of the next convolutional block. The attention module \mathcal{H} is achieved in two stages:

1) *T1 Modulation*: In this stage, we aim to modulate T1 weighted images with powerful attention modules to obtain more informative feature representation. This is achieved with two attention modules, organized in a sequential manner (see Fig. 4):

$$\text{channel attention: } \mathbf{f}_{T_1}^c = \mathcal{H}^c(\mathbf{f}_{T_1}) \in \mathbb{R}^{H \times W \times C}, \quad (8)$$

$$\text{spatial attention: } \mathbf{f}_{T_1}^s = \mathcal{H}^s(\mathbf{f}_{T_1}^c) \in \mathbb{R}^{H \times W \times C}. \quad (9)$$

Here, Eq. (8) is designed based on the famous Squeeze-and-Excitation Network (SENet) [69], which does not rely on extra inputs and is trivial in computational cost. This is because the channel attention aims to reduce the dimensions, while the spatial attention aims to determine the most important information to guide the restoration of the target modality. Thus, if we place the spatial attention before the channel attention, there will be a loss of information [79]. To avoid this, we organize them sequentially as the channel-spatial attention. It re-weights the feature response across channels using the *squeeze* and *excitation* operations. More specifically, the *squeeze* operator acquires global information by aggregating the features across

all the spatial locations through channel-wise global average pooling:

$$\mathbf{z} = P_{\max}(\mathbf{f}_{T_1}) \in \mathbb{R}^C, \quad (10)$$

where P_{\max} indicates the global max pooling operation, and \mathbf{z} is a global statistic. In the *excitation* step, a gating mechanism is employed on the channel-wise descriptor:

$$\mathbf{s} = \sigma(\mathbf{W}_2 \delta(\mathbf{W}_1 \mathbf{z})) \in [0, 1]^C, \quad (11)$$

where σ and δ are *Sigmoid* and *ReLU* functions, respectively. $\mathbf{W}_1 \in \mathbb{R}^{\frac{C}{d} \times C}$ and $\mathbf{W}_2 \in \mathbb{R}^{C \times \frac{C}{d}}$ are two fully-connected (FC) layers with $r > 1$ as the reduction ratio for computational efficiency. Through Eq. (11), we obtain an attention vector \mathbf{s} that encodes non-mutually-exclusive relations among the channels of \mathbf{f}_{T_1} . The \mathbf{s} is then applied to re-weight the channels of the original feature \mathbf{f}_{T_1} :

$$\mathbf{f}_{T_1}^c = [s^1 \cdot \mathbf{f}_{T_1}^1, \dots, s^C \cdot \mathbf{f}_{T_1}^C], \quad (12)$$

where $s^i \in \mathbb{R}$ is the i -th element in \mathbf{s} , and $\mathbf{f}_{T_1}^i \in \mathbb{R}^{H \times W}$ indicates the feature map of i -th channel in \mathbf{f}_{T_1} . ‘[.]’ is a channel-wise concatenation operator.

While the channel attention focuses on highlighting ‘what’ is meaningful in \mathbf{f}_{T_1} [80], we further discover ‘where’ is important in $\mathbf{f}_{T_1}^c$ using a spatial-wise attention module \mathcal{H}^s (Eq. (9)). Formally, we first obtain a spatial attention map \mathbf{m} as follows:

$$\mathbf{m} = \sigma(\text{Conv}(Q_{\max}(\mathbf{f}_{T_1}^c))) \in [0, 1]^{H \times W}, \quad (13)$$

where Q_{\max} represents the global max pooling along the channel axis. A 7×7 convolutional layer is applied to the pooled feature to learn where to emphasize or suppress. Next, we employ \mathbf{m} to enrich the channel-attentive feature $\mathbf{f}_{T_1}^c$:

$$\mathbf{f}_{T_1}^s = \mathbf{f}_{T_1}^c \otimes \mathbf{m}, \quad (14)$$

where \otimes denotes the element-wise multiplication. Through the sequential channel and spatial attention modules, we obtain a more informative feature representation $\mathbf{f}_{T_1}^s$. Next, we use it to enhance the features of the T2 modality.

2) T1-Guided Fusion: Since T1 weighted images are used to guide the reconstruction of T2 weighted images, we use the modulated T1 weighted features as complementary information and fuse them into T2 weighted features. The T1-guided fusion module works in the following residual form:

$$\hat{\mathbf{f}}_{T_2} = \mathbf{f}_{T_2} \otimes \mathbf{f}_{T_1}^s \oplus \mathbf{f}_{T_2}, \quad (15)$$

where \oplus denotes element-wise summation. Thanks to the fusion with T1 modulation, $\hat{\mathbf{f}}_{T_2}$ contains rich complementary information with emphasis on T1 weighted features. By using the T1-guided attention module at each level, we obtain the depth aggregation features.

V. EXPERIMENTS

In this section, we first introduce the details of the multi-modal dataset used in our experiments, and the evaluation metrics. Then, we describe our implementation details and comparison methods. Finally, we perform an ablation study to investigate the aggregation strategies and different modules in our model.

A. Dataset

To validate the effectiveness of our model, we use two multi-modal datasets in our experiments. The first is IXI¹, which consists of 577 subjects with different MR sequences from three different hospitals in London (*i.e.*, Hammersmith Hospital using a Philips 3T system, Guy’s Hospital using a Philips 1.5T system, and Institute of Psychiatry using a GE 1.5T system). In this study, we use the T1 weight images in this dataset to guide T2 image reconstruction. We randomly split the data into 369 subjects for training, 93 subjects for validation, and 115 subjects for testing. Each subject with paired T1 and T2 weighted images and the volume is cropped to a size of $256 \times 256 \times 100$. The second dataset is fastMRI. Following [81], we filter out 8332 and 1665 pairs of PD and PDFS slice for training and validation, respectively. In fastMRI, the PDs are the same as T1, which are the auxiliary modality to guide the reconstruction of the the target modality PDFSs [81]. More details on this dataset can be found on its website². All the datasets are manually aligned before our experiments.

To verify the robustness of our method, in this experiment, we use four different undersampling masks with different acceleration rates to obtain the various undersampled measurements, including 1D Uniform, 1D Random, 2D Radial and 2D Spiral patterns with $3 \times$, $6 \times$, and $9 \times$. Rician noise was also randomly generated with a power of 10% of mean voxel intensities and added to the k -space data before applying the undersampling. Examples of the undersampling patterns are illustrated in the left column in Fig. 5 and Fig. 6. For fastMRI, we use the 1D Random and Equispaced sampling patterns with different acceleration rates provided by the dataset to evaluate our method.

B. Implementation Details

To demonstrate its effectiveness, we compare our method with UNet [82] on single-modal MR image data (UNet-T2), a multi-modal fusion method proposed by Xiang *et al.* [21], and DuDoRNet [22]. Various forms of our method will be discussed in the ablation study. All these methods are trained on the same dataset. For fair comparison, [21] and [22] are retrained using their default parameter settings, where the number of feature maps in [21] is 64. We implement our model in PyTorch and train it on two NVIDIA Tesla V100 GPUs with 32GB of memory per card. Testing is conducted on a single NVIDIA Tesla V100 GPU with a 32GB memory. To reveal full details of our method, our implementations will be released. Our model is fully end-to-end trainable. The parameters are updated using the Adam optimizer [83] with an initial learning rate 0.001. We train the model for 50 epochs in total with a mini-batch size of 8. The α and β in our experiments are empirically set to 0.4, and 0.6, respectively.

C. Evaluation Metrics

We use three popular metrics to evaluate our reconstruction performance: normalized mean square error (NMSE),

¹<http://brain-development.org/ixi-dataset/>

²<https://fastmri.org/leaderboards/>

TABLE I: Average (with standard deviation) results on the IXI dataset under different undersampling patterns, in terms of SSIM, and PSNR. The best and second-best results are marked in red and blue, respectively.

Method	1D-Uniform-6×		1D-Uniform-9×		Method	1D-Random-3×		1D-Random-6×	
	SSIM↑	PSNR↑	SSIM↑	PSNR↑		SSIM↑	PSNR↑	SSIM↑	PSNR↑
ZF	0.756±0.06	25.9±1.93	0.703±0.08	25.9±2.11	ZF	0.747±0.10	27.8±1.73	0.694±0.12	25.9±2.28
UNet-T2	0.897±0.03	29.5±1.01	0.880±0.05	28.3±1.01	UNet-T2	0.926±0.14	32.6±1.02	0.882±0.07	29.3±1.28
Xiang <i>et al.</i>	0.935±0.04	31.5±1.52	0.955±0.08	31.0±1.47	Xiang <i>et al.</i>	0.932±0.08	32.5±1.21	0.920±0.04	31.6±1.09
DuDoRNet	0.937±0.04	32.6±1.72	0.930±0.08	31.8±1.38	DuDoRNet	0.945±0.07	33.9±1.09	0.926±0.07	31.9±1.29
MANet	0.944±0.02	32.9±1.02	0.947±0.04	32.4±1.16	MANet	0.969±0.06	36.9±1.18	0.949±0.04	33.1±1.02
Method	2D-Radial-6×		2D-Radial-9×		Method	2D-Spiral-6×		2D-Spiral-9×	
	SSIM↑	PSNR↑	SSIM↑	PSNR↑		SSIM↑	PSNR↑	SSIM↑	PSNR↑
ZF	0.487±0.08	27.1±1.86	0.414±0.07	25.2±1.28	ZF	0.617±0.06	28.1±1.28	0.638±0.07	27.6±2.12
UNet-T2	0.894±0.06	31.3±1.09	0.853±0.06	28.8±1.17	UNet-T2	0.894±0.06	31.2±1.42	0.883±0.04	30.4±1.08
Xiang <i>et al.</i>	0.905±0.08	32.3±1.68	0.890±0.08	30.5±1.72	Xiang <i>et al.</i>	0.905±0.05	31.8±1.07	0.890±0.03	30.6±1.21
DuDoRNet	0.931±0.06	33.3±1.02	0.912±0.06	31.5±1.27	DuDoRNet	0.942±0.04	34.1±1.27	0.939±0.05	33.1±1.65
MANet	0.947±0.07	34.3±1.31	0.927±0.05	32.9±1.11	MANet	0.951±0.04	34.5±1.17	0.940±0.03	33.0±1.20

TABLE II: Average (with standard deviation) results on the fastMRI dataset under different undersampling patterns, in terms of SSIM, and PSNR. The best and second-best results are marked in red and blue, respectively.

Method	Random-4×		Random-8×		Method	Equispaced-4×		Equispaced-8×	
	SSIM↑	PSNR↑	SSIM↑	PSNR↑		SSIM↑	PSNR↑	SSIM↑	PSNR↑
UNet-PDFS	0.630±0.04	29.2±1.55	0.550±0.02	28.1±1.07	UNet-PDFS	0.600±0.06	29.2±1.52	0.553±0.06	28.2±1.15
Xiang <i>et al.</i>	0.600±0.05	29.3±1.54	0.562±0.06	28.4±1.25	Xiang <i>et al.</i>	0.621±0.05	29.4±1.71	0.567±0.03	28.6±1.10
DuDoRNet	0.640±0.02	29.5±1.33	0.571±0.05	28.7±1.38	DuDoRNet	0.641±0.05	29.6±1.39	0.577±0.05	28.8±1.29
MANet	0.652±0.02	30.3±1.12	0.604±0.05	29.4±1.09	MANet	0.646±0.03	30.4±1.22	0.588±0.04	29.6±1.19

structural similarity (SSIM) and peak signal-to-noise ratio (PSNR) [84]. Given a reconstructed image as vector \hat{v} and a reference image as v , we can formulate NMSE and PSNR as follows:

$$\text{NMSE}(\hat{v}, v) = \frac{\|\hat{v} - v\|_2^2}{\|v\|_2^2}, \quad (16)$$

$$\text{PSNR}(\hat{v}, v) = 10 \log_{10} \frac{\max(v)^2}{\text{MSE}(\hat{v}, v)}, \quad (17)$$

where $\|\cdot\|_2^2$ is the squared Euclidean norm, and the subtraction is performed entry-wise, $\max(v)$ represents the largest entry in the ground truth, and $\text{MSE}(\hat{v}, v)$ represents the mean square error between \hat{v} and v . NMSE evaluates structural properties of the objects in an image by exploiting the inter-dependencies among nearby pixels. Given two image patches \hat{m} and m , we have

$$\text{SSIM}(\hat{m}, m) = \frac{(2\mu_{\hat{m}}\mu_m + c_1)(2\sigma_{\hat{m}m} + c_2)}{(\mu_{\hat{m}}^2 + \mu_m^2 + c_1)(\sigma_{\hat{m}}^2 + \sigma_m^2 + c_2)} \quad (18)$$

where $\mu_{\hat{m}}$ and μ_m are the average pixel intensities, $\sigma_{\hat{m}m}$ is their covariance, $\sigma_{\hat{m}}^2$ and σ_m^2 are their variances, and c_1 and c_2 are two variables to stabilize the division. Higher values of PSNR and SSIM, lower values of NMSE indicate a better reconstruction.

D. Quantitative Results

We evaluate the reconstruction of T2 weighted images under the guidance of T1 weighted features in Table I, and the reconstruction PDFS images under the guidance of PD features in

Table II. Each reports the average SSIM and PSNR scores with respect to different undersampling patterns and acceleration factors. The first two sub-tables summarize the image quality under 1D Uniform and 1D Random sampling patterns with different acceleration rates. We find that our MANet with these two undersampling pattern yields the best results among all sampling patterns and reconstruction methods. This suggests that our model can effectively fuse the T1 weight features from the complementary modality, and that this is beneficial to the reconstruction of the target modality. Specifically, without the guidance of T1 weight data, the restoration of the T2 weight image is far less effective than when using other multi-modal fusion models.

Although [21] also adds the T1 weight information into the model, it directly concatenate the T1 and T2 weights together as the input of the network, rather than explicitly learn the characteristics of T1 weight to help the T2 reconstruction. Therefore, its performance is less effective in comparison with other fusion models. In particular, under the 1D Random sampling mask with 3× acceleration, we improve the PSNR from 33.929 dB to 36.927 dB, and SSIM from 0.945 to 0.969, as compared to current best approach, *i.e.*, DuDoRNet. Since DuDoRNet and Xiang *et al.* only use the auxiliary modality as prior information, without any changes in the network, they have fewer parameters than our method. However, their reconstruction results are inferior to those produced by our model. Under 2D Radial undersampling patterns, our MANet achieves scores 34.317 and 32.872 in terms of PSNR at 6× and 9× acceleration rates, respectively. Moreover, our model also

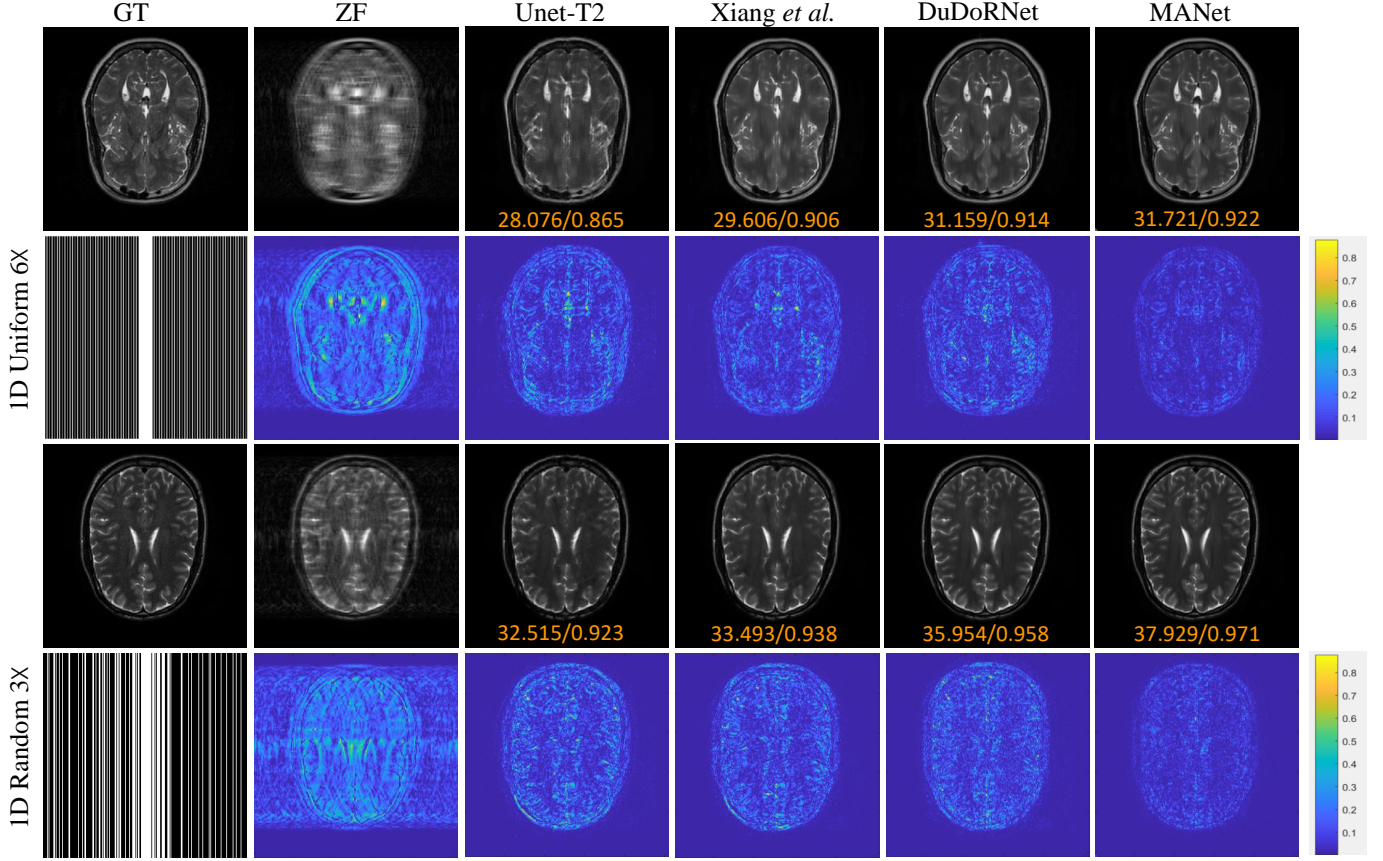


Fig. 5: Visual comparison of different methods under **1D undersampling patterns** with **3 \times** and **6 \times** acceleration rate. Reconstruction results and error maps are presented with corresponding quantitative measurements in PSNR/SSIM.

TABLE III: Ablative results on the IXI dataset under different undersampling patterns, in terms of SSIM, and PSNR. The best and second-best results are marked in red and blue, respectively.

Method	1D-Uniform-6 \times		1D-Uniform-9 \times	
	SSIM \uparrow	PSNR \uparrow	SSIM \uparrow	PSNR \uparrow
w/o k -space	0.937\pm0.02	32.1\pm1.04	0.934\pm0.15	31.5 \pm 1.46
w/o T1-GA	0.935 \pm 0.05	30.2 \pm 1.26	0.934\pm0.04	31.8\pm1.37
MANet	0.944\pm0.02	32.9\pm1.02	0.947\pm0.04	32.4\pm1.16
Method	2D-Radial-6 \times		2D-Radial-9 \times	
	SSIM \uparrow	PSNR \uparrow	SSIM \uparrow	PSNR \uparrow
w/o k -space	0.903 \pm 0.07	31.1 \pm 1.54	0.915\pm0.07	30.8\pm1.50
w/o T1-GA	0.930\pm0.07	32.6\pm1.49	0.904 \pm 0.06	28.9 \pm 1.53
MANet	0.947\pm0.07	34.3\pm1.31	0.927\pm0.05	32.9\pm1.11

achieves compelling performance under the 2D Spiral patterns.

Although the reconstructions with zero filling (ZF) at a high acceleration rate create significant aliasing artifacts and lose anatomical details, our MANet still achieve the highest PSNR and SSIM values, and lowest NMSE values. UNet-T2 without fusion of T1 weight features can improve the reconstruction as compared to ZF, but it is hard to see a significant improvement when a high undersampling rate is presented. Additionally, it is obvious that 1D undersampling patterns make the image more difficult to restore than when using 2D patterns, and the reconstruction becomes more difficult when the acceleration rate increases. However, our method still outperforms

Method	1D-Random-3 \times		1D-Random-6 \times	
	SSIM \uparrow	PSNR \uparrow	SSIM \uparrow	PSNR \uparrow
w/o k -space	0.961 \pm 0.07	34.2 \pm 1.33	0.926 \pm 0.06	31.3 \pm 1.40
w/o T1-GA	0.965\pm0.06	36.5\pm1.37	0.935\pm0.02	32.8\pm1.04
MANet	0.969\pm0.06	36.9\pm1.18	0.949\pm0.04	33.1\pm1.02
Method	2D-Spiral-6 \times		2D-Spiral-9 \times	
	SSIM \uparrow	PSNR \uparrow	SSIM \uparrow	PSNR \uparrow
w/o k -space	0.911 \pm 0.04	30.1 \pm 1.22	0.934\pm0.03	30.2 \pm 1.10
w/o T1-GA	0.950\pm0.04	34.1\pm1.13	0.934\pm0.03	30.3\pm1.15
MANet	0.951\pm0.04	34.5\pm1.17	0.940\pm0.03	33.0\pm1.20

previous methods under extremely challenging settings (*i.e.*, 1D masks with 9 \times acceleration). This can be attributed to the powerful capability of our multi-scale fusion model both in the frequency and image domain. More importantly, the overall results in Table I reveal the strong robustness of our multi-scale fusion model under various undersampling patterns and acceleration rates.

E. Visual Comparison

For visual comparison, we depict the reconstructed T2 weight images and corresponding error maps under 1D Uniform and Random patterns with 3 \times and 6 \times acceleration rates

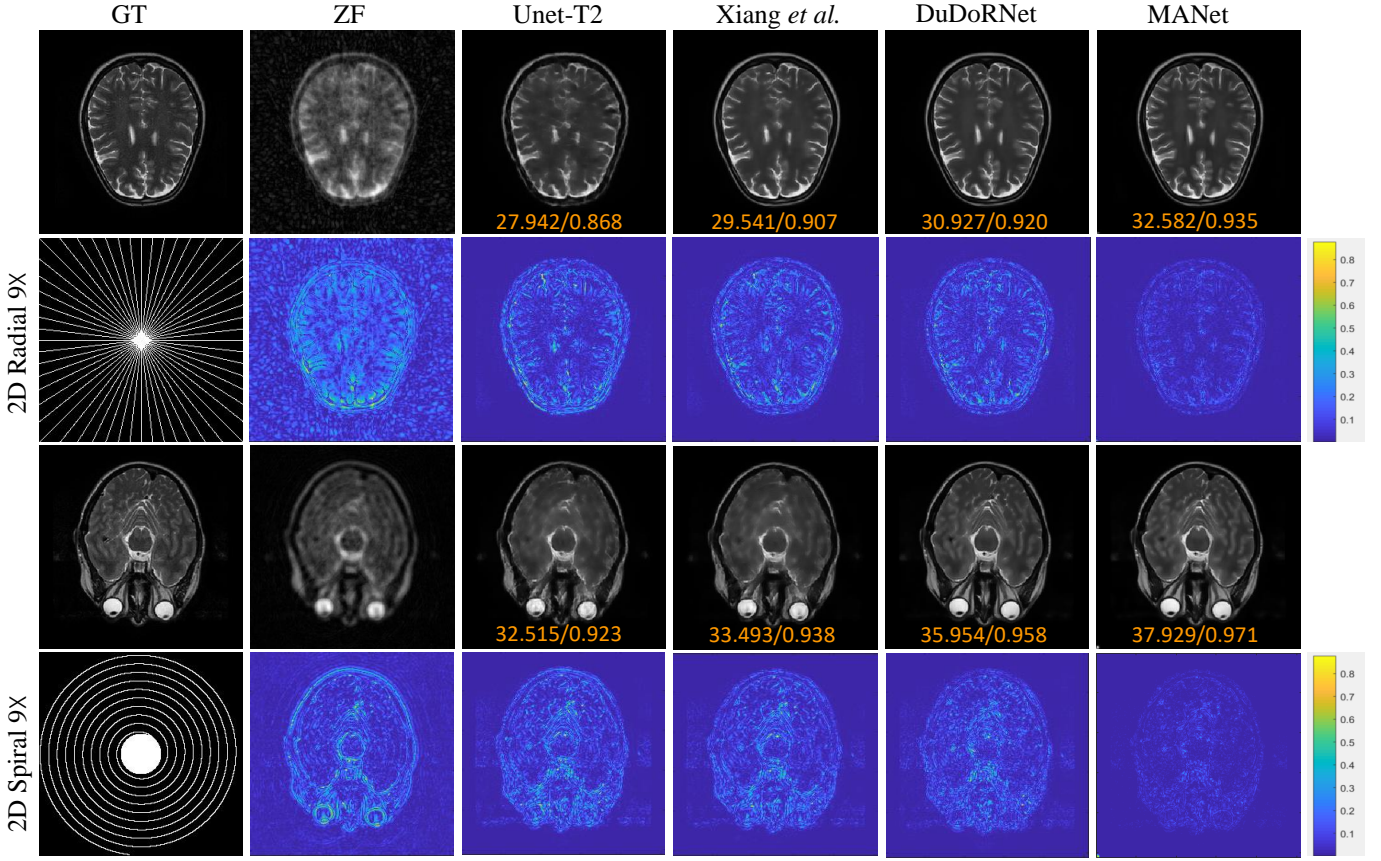


Fig. 6: Visual comparison of different methods under **2D undersampling patterns** with $9\times$ acceleration rate. Reconstruction results and error maps are presented with corresponding quantitative measurements in PSNR/SSIM.

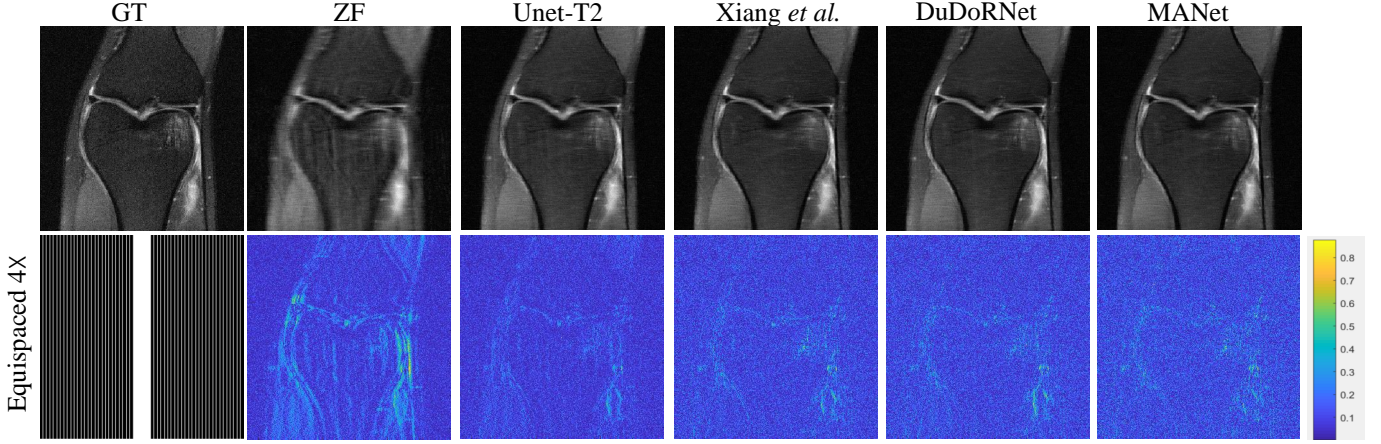


Fig. 7: Visual comparison of different methods on fastMRI under **Equispaced undersampling patterns** with $4\times$ acceleration rate.

in Fig. 5. It is obvious that the restoration of ZF creates severe aliasing artifacts and fake details. UNet-T2 can improve the reconstruction as compared to ZF, but it still produces poor results than other T1 weight fusion methods. Our reconstructions exhibit less aliasing artifacts and structural losses as compared to other methods. More importantly, our method is robust under various undersampling patterns and acceleration rates, achieving better results and better-preserved anatomical details especially at a high acceleration rate.

We next display the reconstructed T2 weight images and corresponding error maps under 2D Radial and Spiral patterns with $6\times$ and $9\times$ acceleration rates in Fig. 6. In general, 2D undersampling masks provide better results in comparison to 1D undersampling masks. As shown in the figure, the images reconstructed by our method have fewer reconstruction errors and clearer structures than those produced by other methods. The superior performance is owed to the fact that our method can effectively aggregate the features of T1 and T2 images

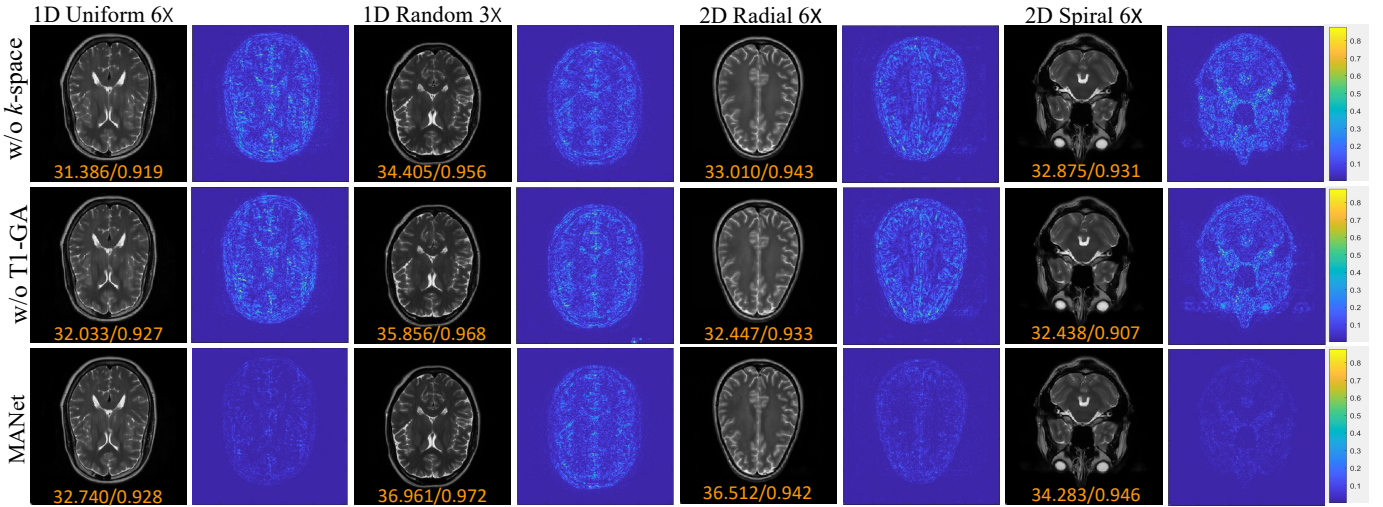


Fig. 8: Reconstruction results from 1D Uniform $6\times$, 1D Random $3\times$, 2D Radial $6\times$ and 2D Spiral $6\times$. Reconstruction results and error maps are presented with corresponding quantitative measurements in PSNR/SSIM.

TABLE IV: Different combinations of channel and spatial attentions. SC represents the sequential spatial and channel attentions, CS represents the sequential channel and spatial attentions, and the SC-CS represents the combine of the SC and CS.

Variant	SC		CS		SC-CS	
	SSIM	PSNR	SSIM	PSNR	SSIM	PSNR
	0.934	32.535	0.944	32.903	0.936	32.815

in various scales. Fig. 7 displays the reconstructed PDFS and the corresponding error maps under Equispaced patterns with $4\times$ acceleration rate. It shows that our method provides clear anatomical details and less aliasing artifacts.

F. Ablation Study

In this section, we conduct ablative experiments to evaluate the effectiveness of the essential components in our model. We design two baseline models: w/o k -space which only employs image-domain data for reconstruction, as well as w/o T1-GA which directly concatenates the features of the two modalities rather than aggregation using the attention module.

Without loss of generality, the reconstruction performance is evaluated on 1D Uniform, 1D Random, 2D Radial, 2D Spiral patterns with acceleration rates of $3\times$, $6\times$, and $9\times$. The results are summarized in Table III. From the table, we observe that w/o k -space and w/o T1-GA are worse than our complete model. This indicates the importance of k -space information for the reconstruction, and that learning from two domains is necessary to achieve complementary representations, even when using simple fusion strategies. More importantly, MANet further improve the results of w/o T1-GA and w/o k -space on all undersampling patterns and acceleration rates, showing the powerful capability of our T1-guided attention module in selectively discovering crucial information to guide T2 weighted image reconstruction.

For qualitative analysis, we visually show the reconstruction results with error maps in Fig. 8. It obvious that our MANet

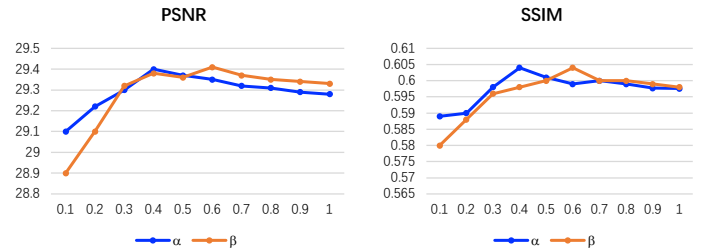


Fig. 9: Ablation study about α and β in terms of PSNR and SSIM.

can restore the image details with minimum errors for all undersampling patterns and acceleration rates. Combining the T1-guided attention module and hybrid domain learning, our model leads to the highest boost in performance. Our MANet, equipping with all components, produces the best reconstruction results with minimum error. Notably, on the Spiral pattern with $6\times$ acceleration rate, the reconstructed image of our full model is extremely high-quality, even in comparison with ground truth images.

Secondly, to demonstrate the effectiveness of our T1-GA module, we provide a comparison with different combinations of channel and spatial attentions in Table IV, where SC represents the sequential spatial and channel attentions, CS represents the sequential channel and spatial attentions, and SC-CS represents the combination of SC and CS. From this table, we find that the results of CS are comparable with SC-CS, while the results of SC are worse. This is consistent with what we mentioned before. CS can first reduce the dimensions and then filter the important information guiding the target modal recovery, to avoid the loss of information. Furthermore, to avoid increasing the number parameters, even by just a few, CS is the best combination for our T1-GA module.

Thirdly, we record the reconstruction results of our method on fastMRI dataset under Equispaced undersampling patterns with $4\times$ acceleration rat in Fig. 9, to evaluate the the influence

of α and β between the two modalities and two domains. The weight between the two modalities is determined by the value of α , and the weight between the two domains is determined by the value of β . The greater the value of α , the greater the proportion in the frequency domain. Similarly, the greater the value of β , the greater the proportion of auxiliary modality. Fig. 9 shows our model achieves the best PSNR and SSIM scores at $\alpha = 0.4$ and $\beta = 0.6$, which means both the auxiliary modality and k -space domain plays an important role in our model. But when α and β smaller than 0.4, the reconstruction performance quickly degrades, and especially when α goes down. This shows that the auxiliary mode plays an important role in our method.

VI. CONCLUSION

In this paper, we focus on the multi-modal fusion for fast MR image reconstruction. For this purpose, we propose a novel end-to-end multi-modal fusion network to deal with different MR sequences in an effective way. Specifically, our method explores the modality-specific properties within each modality to guide the final T2 weight image reconstruction. Besides, a T1-guided attention module is designed to effectively fuse the T1 and T2 weight features at each convolutional stage for multi-scale learning. Moreover, we also adopt a hybrid domain learning network to simultaneously restore the image details in both frequency and image domains. We conduct extensive experiments on multi-modal MR image datasets under different undersampling patterns and acceleration rates, and the results demonstrate that our proposed model significantly outperforms other state-of-the-art synthesis methods.

REFERENCES

- [1] P. C. Lauterbur, “Image formation by induced local interactions: examples employing nuclear magnetic resonance,” *nature*, vol. 242, no. 5394, pp. 190–191, 1973. [1](#)
- [2] D. Moratal, A. Vallés-Luch, L. Martí-Bonmatí, and M. E. Brummer, “ k -space tutorial: an mri educational tool for a better understanding of k -space,” *Biomedical imaging and intervention journal*, vol. 4, no. 1, 2008. [1](#)
- [3] Z. Zhang, A. Romero, M. J. Muckley, P. Vincent, L. Yang, and M. Drozdal, “Reducing uncertainty in undersampled mri reconstruction with active acquisition,” in *IEEE Conf. Comput. Vis. Pattern Recog.*, 2019, pp. 2049–2058. [1, 2, 3](#)
- [4] S. Hu, Y. Shen, S. Wang, and B. Lei, “Brain mr to pet synthesis via bidirectional generative adversarial network,” in *International Conference on Medical Image Computing and Computer-Assisted Intervention*. Springer, 2020, pp. 698–707. [1](#)
- [5] L. Xiang, Y. Qiao, D. Nie, L. An, W. Lin, Q. Wang, and D. Shen, “Deep auto-context convolutional neural networks for standard-dose pet image estimation from low-dose pet/mri,” *Neurocomputing*, vol. 267, pp. 406–416, 2017. [1](#)
- [6] C. Y. Lin and J. A. Fessler, “Efficient dynamic parallel mri reconstruction for the low-rank plus sparse model,” *IEEE transactions on computational imaging*, vol. 5, no. 1, pp. 17–26, 2018. [1](#)
- [7] R. S. Mathew and J. S. Paul, “Sparsity promoting adaptive regularization for compressed sensing parallel mri,” *IEEE Transactions on Computational Imaging*, vol. 4, no. 1, pp. 147–159, 2017. [1](#)
- [8] Y. Yang, J. Sun, H. Li, and Z. Xu, “Admm-csnet: A deep learning approach for image compressive sensing,” *IEEE Trans. Pattern Anal. Mach. Intell.*, vol. 42, no. 3, pp. 521–538, 2020. [1, 2, 3](#)
- [9] M. Lustig, D. Donoho, and J. M. Pauly, “Sparse mri: The application of compressed sensing for rapid mr imaging,” *Magnetic Resonance in Medicine: An Official Journal of the International Society for Magnetic Resonance in Medicine*, vol. 58, no. 6, pp. 1182–1195, 2007. [1, 3](#)
- [10] K. P. Pruessmann, M. Weiger, M. B. Scheidegger, and P. Boesiger, “Sense: sensitivity encoding for fast mri,” *Magnetic Resonance in Medicine: An Official Journal of the International Society for Magnetic Resonance in Medicine*, vol. 42, no. 5, pp. 952–962, 1999. [1](#)
- [11] M. A. Griswold, P. M. Jakob, R. M. Heidemann, M. Nittka, V. Jellus, J. Wang, B. Kiefer, and A. Haase, “Generalized autocalibrating partially parallel acquisitions (grappa),” *Magnetic Resonance in Medicine: An Official Journal of the International Society for Magnetic Resonance in Medicine*, vol. 47, no. 6, pp. 1202–1210, 2002. [1, 3](#)
- [12] K. Wu, Y. Guo, and C. Zhang, “Compressing deep neural networks with sparse matrix factorization,” *IEEE Transactions on Neural Networks and Learning Systems*, 2019. [1](#)
- [13] S. Yu, H. Dong, G. Yang, G. Slabaugh, P. L. Dragotti, X. Ye, F. Liu, S. Arridge, J. Keegan, D. Firmin *et al.*, “Deep de-aliasing for fast compressive sensing mri,” *arXiv preprint arXiv:1705.07137*, 2017. [1](#)
- [14] M. Hutchinson and U. Raff, “Fast mri data acquisition using multiple detectors,” *Magnetic resonance in Medicine*, vol. 6, no. 1, pp. 87–91, 1988. [1](#)
- [15] S. Wang, Z. Su, L. Ying, X. Peng, S. Zhu, F. Liang, D. Feng, and D. Liang, “Accelerating magnetic resonance imaging via deep learning,” *IEEE International Symposium on Biomedical Imaging*, pp. 514–517, 2016. [2, 3](#)
- [16] G. Yang, S. Yu, H. Dong, G. Slabaugh, P. L. Dragotti, X. Ye, F. Liu, S. Arridge, J. Keegan, Y. Guo *et al.*, “Dagan: Deep de-aliasing generative adversarial networks for fast compressed sensing mri reconstruction,” *IEEE Trans. on Medical Imaging*, vol. 37, no. 6, pp. 1310–1321, 2017. [2, 3](#)
- [17] T. M. Quan, T. Nguyen-Duc, and W.-K. Jeong, “Compressed sensing mri reconstruction using a generative adversarial network with a cyclic loss,” *IEEE Trans. on Medical Imaging*, vol. 37, no. 6, pp. 1488–1497, 2018. [2, 3](#)
- [18] A. Sriram, J. Zbontar, T. Murrell, C. L. Zitnick, A. Deffazio, and D. K. Sodickson, “Grappanet: Combining parallel imaging with deep learning for multi-coil mri

reconstruction,” in *IEEE Conf. Comput. Vis. Pattern Recog.*, 2020, pp. 14315–14322. [2](#) [3](#)

[19] A. Elazab, C. Wang, S. J. S. Gardezi, H. Bai, Q. Hu, T. Wang, C. Chang, and B. Lei, “Gp-gan: Brain tumor growth prediction using stacked 3d generative adversarial networks from longitudinal mr images,” *Neural Networks*, vol. 132, pp. 321–332, 2020. [2](#)

[20] M. Hamghalam, T. Wang, and B. Lei, “High tissue contrast image synthesis via multistage attention-gan: Application to segmenting brain mr scans,” *Neural Networks*, vol. 132, pp. 43–52, 2020. [2](#)

[21] L. Xiang, Y. Chen, W. Chang, Y. Zhan, W. Lin, Q. Wang, and D. Shen, “Deep-learning-based multi-modal fusion for fast mr reconstruction,” *IEEE Transactions on Biomedical Engineering*, vol. 66, no. 7, pp. 2105–2114, 2018. [2](#) [3](#) [6](#) [7](#)

[22] B. Zhou and S. K. Zhou, “Dudornet: Learning a dual-domain recurrent network for fast mri reconstruction with deep t1 prior,” in *IEEE Conf. Comput. Vis. Pattern Recog.*, 2020, pp. 4273–4282. [2](#) [3](#) [6](#)

[23] B. Yaman, S. Weingärtner, N. Kargas, N. D. Sidiropoulos, and M. Akçakaya, “Low-rank tensor models for improved multidimensional mri: Application to dynamic cardiac t_1 mapping,” *IEEE transactions on computational imaging*, vol. 6, pp. 194–207, 2019. [3](#)

[24] M. Lustig, D. L. Donoho, J. M. Santos, and J. M. Pauly, “Compressed sensing mri,” *IEEE signal processing magazine*, vol. 25, no. 2, pp. 72–82, 2008. [3](#)

[25] Y. Chen, T. Xiao, C. Li, Q. Liu, and S. Wang, “Model-based convolutional de-aliasing network learning for parallel mr imaging,” in *International Conference on Medical Image Computing and Computer-Assisted Intervention*, 2019, pp. 30–38. [3](#)

[26] R. Zhang, H. Zhang, X. Li, and F. Nie, “Adaptive robust low-rank 2-d reconstruction with steerable sparsity,” *IEEE Transactions on Neural Networks and Learning Systems*, 2019. [3](#)

[27] Z. Lai, X. Qu, Y. Liu, G. Di, and C. Zhong, “Image reconstruction of compressed sensing mri using graph-based redundant wavelet transform,” *Medical Image Analysis*, vol. 27, p. 93, 2016. [3](#)

[28] J. Yao, Z. Xu, X. Huang, and J. Huang, “An efficient algorithm for dynamic mri using low-rank and total variation regularizations,” *Medical Image Analysis*, vol. 44, pp. 14–27, 2018. [3](#)

[29] W. Luo, J. Li, J. Yang, W. Xu, and J. Zhang, “Convolutional sparse autoencoders for image classification,” *IEEE transactions on neural networks and learning systems*, vol. 29, no. 7, pp. 3289–3294, 2017. [3](#)

[30] X. Qu, X. Cao, D. Guo, C. Hu, and Z. Chen, “Combined sparsifying transforms for compressed sensing mri,” *Electronics letters*, vol. 46, no. 2, pp. 121–123, 2010. [3](#)

[31] Y. Zhang, Z. Dong, P. Phillips, S. Wang, G. Ji, and J. Yang, “Exponential wavelet iterative shrinkage thresholding algorithm for compressed sensing magnetic resonance imaging,” *Information Sciences*, vol. 322, pp. 115–132, 2015. [3](#)

[32] K. Muhammad, S. Khan, J. Del Ser, and V. H. C. de Albuquerque, “Deep learning for multigrade brain tumor classification in smart healthcare systems: A prospective survey,” *IEEE Transactions on Neural Networks and Learning Systems*, 2020. [3](#)

[33] Q. Liu, Q. Yang, H. Cheng, S. Wang, M. Zhang, and D. Liang, “Highly undersampled magnetic resonance imaging reconstruction using autoencoding priors,” *Magnetic resonance in medicine*, vol. 83, no. 1, pp. 322–336, 2020. [3](#)

[34] Z. Li, Z. Zhang, J. Qin, Z. Zhang, and L. Shao, “Discriminative fisher embedding dictionary learning algorithm for object recognition,” *IEEE transactions on neural networks and learning systems*, vol. 31, no. 3, pp. 786–800, 2019. [3](#)

[35] X. Qu, W. Zhang, D. Guo, C. Cai, S. Cai, and Z. Chen, “Iterative thresholding compressed sensing mri based on contourlet transform,” *Inverse Problems in Science and Engineering*, vol. 18, no. 6, pp. 737–758, 2010. [3](#)

[36] K. Hammernik, T. Klatzer, E. Kobler, M. P. Recht, D. K. Sodickson, T. Pock, and F. Knoll, “Learning a variational network for reconstruction of accelerated mri data,” *Magnetic resonance in medicine*, vol. 79, no. 6, pp. 3055–3071, 2018. [3](#)

[37] H. K. Aggarwal, M. P. Mani, and M. Jacob, “Modl: Model-based deep learning architecture for inverse problems,” *IEEE Trans. on Medical Imaging*, vol. 38, no. 2, pp. 394–405, 2018. [3](#)

[38] H. Wang, R. Feng, Z.-F. Han, and C.-S. Leung, “Admm-based algorithm for training fault tolerant rbf networks and selecting centers,” *IEEE transactions on neural networks and learning systems*, vol. 29, no. 8, pp. 3870–3878, 2017. [3](#)

[39] C. M. Hyun, H. P. Kim, S. M. Lee, S. Lee, and J. K. Seo, “Deep learning for undersampled mri reconstruction,” *Physics in Medicine & Biology*, vol. 63, no. 13, p. 135007, 2018. [3](#)

[40] K. H. Jin, M. T. McCann, E. Froustey, and M. Unser, “Deep convolutional neural network for inverse problems in imaging,” *IEEE Trans. Image Process.*, vol. 26, no. 9, pp. 4509–4522, 2017. [3](#)

[41] B. Zhu, J. Z. Liu, S. F. Cauley, B. R. Rosen, and M. S. Rosen, “Image reconstruction by domain-transform manifold learning,” *Nature*, vol. 555, no. 7697, pp. 487–492, 2018. [3](#)

[42] Y. Han, J. Yoo, H. H. Kim, H. J. Shin, K. Sung, and J. C. Ye, “Deep learning with domain adaptation for accelerated projection-reconstruction mr,” *Magnetic resonance in medicine*, vol. 80, no. 3, pp. 1189–1205, 2018. [3](#)

[43] D. Lee, J. Yoo, S. Tak, and J. C. Ye, “Deep residual learning for accelerated mri using magnitude and phase networks,” *IEEE Transactions on Biomedical Engineering*, vol. 65, no. 9, pp. 1985–1995, 2018. [3](#)

[44] M. Mardani, E. Gong, J. Y. Cheng, S. S. Vasanawala, G. Zaharchuk, L. Xing, and J. M. Pauly, “Deep generative adversarial neural networks for compressive sensing mri,” *IEEE Trans. on Medical Imaging*, vol. 38, no. 1,

pp. 167–179, 2018. 3

[45] L. Sun, Z. Fan, Y. Huang, X. Ding, and J. Paisley, “Compressed sensing mri using a recursive dilated network,” in *AAAI*, 2018. 3

[46] B. Yaman, S. A. H. Hosseini, S. Moeller, J. Ellermann, K. Ugurbil, and M. Akçakaya, “Self-supervised physics-based deep learning mri reconstruction without fully-sampled data,” in *IEEE International Symposium on Biomedical Imaging*, 2020, pp. 921–925. 3

[47] S. Wang, Z. Ke, H. Cheng, S. Jia, L. Ying, H. Zheng, and D. Liang, “Dimension: dynamic mr imaging with both k-space and spatial prior knowledge obtained via multi-supervised network training,” *NMR in Biomedicine*, p. e4131, 2019. 3

[48] T. Eo, Y. Jun, T. Kim, J. Jang, H.-J. Lee, and D. Hwang, “Kiki-net: cross-domain convolutional neural networks for reconstructing undersampled magnetic resonance images,” *Magnetic resonance in medicine*, vol. 80, no. 5, pp. 2188–2201, 2018. 3

[49] W. Zhang, H. Zhou, S. Sun, Z. Wang, J. Shi, and C. C. Loy, “Robust multi-modality multi-object tracking,” in *Int. Conf. Comput. Vis.*, 2019, pp. 2365–2374. 3

[50] J. Duan, S. Zhou, J. Wan, X. Guo, and S. Z. Li, “Multi-modality fusion based on consensus-voting and 3d convolution for isolated gesture recognition,” *arXiv preprint arXiv:1611.06689*, 2016. 3

[51] N. Audebert, B. Le Saux, and S. Lefèvre, “Semantic segmentation of earth observation data using multimodal and multi-scale deep networks,” in *Asi. Conf. Comput. Vis.*, 2016, pp. 180–196. 3

[52] A. Valada, R. Mohan, and W. Burgard, “Self-supervised model adaptation for multimodal semantic segmentation,” *Int. J. Comput. Vis.*, pp. 1–47, 2019. 3

[53] X. Zhuang and J. Shen, “Multi-scale patch and multi-modality atlases for whole heart segmentation of mri,” *Medical Image Analysis*, p. 77, 2016. 3

[54] S. Bahrampour, N. M. Nasrabadi, A. Ray, and W. K. Jenkins, “Multimodal task-driven dictionary learning for image classification,” *IEEE Trans. Image Process.*, vol. 25, no. 1, pp. 24–38, 2015. 3

[55] H. Nam, J.-W. Ha, and J. Kim, “Dual attention networks for multimodal reasoning and matching,” in *IEEE Conf. Comput. Vis. Pattern Recog.*, 2017, pp. 299–307. 3

[56] X. Huang, M.-Y. Liu, S. Belongie, and J. Kautz, “Multi-modal unsupervised image-to-image translation,” in *Eur. Conf. Comput. Vis.*, 2018, pp. 172–189. 3

[57] D. Nie, H. Zhang, E. Adeli, L. Liu, and D. Shen, “3d deep learning for multi-modal imaging-guided survival time prediction of brain tumor patients,” in *International conference on medical image computing and computer-assisted intervention*, 2016, pp. 212–220. 3

[58] H. Fan, X. Mei, D. Prokhorov, and H. Ling, “Rgb-d scene labeling with multimodal recurrent neural networks,” in *Proceedings of the IEEE Conference on Computer Vision and Pattern Recognition (CVPR) Workshops*, July 2017. 3

[59] T. Zhou, H. Fu, G. Chen, J. Shen, and L. Shao, “Hinet: hybrid-fusion network for multi-modal mr image synthesis,” *IEEE Trans. on Medical Imaging*, 2020. 3

[60] M. Marcinkiewicz, J. Nalepa, P. R. Lorenzo, W. Dudzik, and G. Mrukwa, “Segmenting brain tumors from mri using cascaded multi-modal u-nets,” in *International MICCAI Brainlesion Workshop*. Springer, 2018, pp. 13–24. 3

[61] Q. Dou, Q. Liu, P. A. Heng, and B. Glocker, “Unpaired multi-modal segmentation via knowledge distillation,” *arXiv preprint arXiv:2001.03111*, 2020. 3

[62] M. J. Ehrhardt, K. Thielemans, L. Pizarro, D. Atkinson, S. Ourselin, B. F. Hutton, and S. R. Arridge, “Joint reconstruction of pet-mri by exploiting structural similarity,” *Inverse Problems*, vol. 31, no. 1, p. 015001, 2014. 3

[63] F. Knoll, M. Holler, T. Koesters, R. Otazo, K. Bredies, and D. K. Sodickson, “Joint mr-pet reconstruction using a multi-channel image regularizer,” *IEEE transactions on medical imaging*, vol. 36, no. 1, pp. 1–16, 2016. 3

[64] H. Zhang, K. Dana, J. Shi, Z. Zhang, X. Wang, A. Tyagi, and A. Agrawal, “Context encoding for semantic segmentation,” in *IEEE Conf. Comput. Vis. Pattern Recog.*, 2018, pp. 7151–7160. 4

[65] C. Yu, J. Wang, C. Peng, C. Gao, G. Yu, and N. Sang, “Learning a discriminative feature network for semantic segmentation,” in *IEEE Conf. Comput. Vis. Pattern Recog.*, 2018, pp. 1857–1866. 4

[66] T. Dai, J. Cai, Y. Zhang, S.-T. Xia, and L. Zhang, “Second-order attention network for single image super-resolution,” in *IEEE Conf. Comput. Vis. Pattern Recog.*, 2019, pp. 11 065–11 074. 4

[67] J. Shen, X. Tang, X. Dong, and L. Shao, “Visual object tracking by hierarchical attention siamese network,” *IEEE Trans on Cybernetics*, 2019. 4

[68] F. Wang, M. Jiang, C. Qian, S. Yang, C. Li, H. Zhang, X. Wang, and X. Tang, “Residual attention network for image classification,” in *IEEE Conf. Comput. Vis. Pattern Recog.*, 2017, pp. 3156–3164. 4

[69] J. Hu, L. Shen, and G. Sun, “Squeeze-and-excitation networks,” in *IEEE Conf. Comput. Vis. Pattern Recog.*, 2018, pp. 7132–7141. 4, 5

[70] A. Zhang, L. Yue, J. Shen, F. Zhu, X. Zhen, X. Cao, and L. Shao, “Attentional neural fields for crowd counting,” in *Int. Conf. Comput. Vis.*, 2019, pp. 5714–5723. 4

[71] J. Lu, J. Yang, D. Batra, and D. Parikh, “Hierarchical question-image co-attention for visual question answering,” in *Adv. Neural Inform. Process. Syst.*, 2016, pp. 289–297. 4

[72] Q. Huang, D. Yang, P. Wu, H. Qu, J. Yi, and D. Metaxas, “Mri reconstruction via cascaded channel-wise attention network,” in *International Symposium on Biomedical Imaging (ISBI 2019)*. IEEE, 2019, pp. 1622–1626. 4

[73] L. Luo, H. Chen, X. Wang, Q. Dou, H. Lin, J. Zhou, G. Li, and P.-A. Heng, “Deep angular embedding and feature correlation attention for breast mri cancer analysis,” in *International Conference on Medical Image Computing and Computer-Assisted Intervention*. Springer, 2019, pp. 504–512. 4

[74] G. Wang, J. Shapey, W. Li, R. Dorent, A. Demetriadis, S. Bisdas, I. Paddick, R. Bradford, S. Zhang, S. Ourselin

et al., “Automatic segmentation of vestibular schwannoma from t2-weighted mri by deep spatial attention with hardness-weighted loss,” in *International Conference on Medical Image Computing and Computer-Assisted Intervention*. Springer, 2019, pp. 264–272. 4

[75] L. Li, X. Weng, J. A. Schnabel, and X. Zhuang, “Joint left atrial segmentation and scar quantification based on a dnn with spatial encoding and shape attention,” in *International Conference on Medical Image Computing and Computer-Assisted Intervention*. Springer, 2020, pp. 118–127. 4

[76] C. Liu, W. Ding, L. Li, Z. Zhang, C. Pei, L. Huang, and X. Zhuang, “Brain tumor segmentation network using attention-based fusion and spatial relationship constraint,” *arXiv preprint arXiv:2010.15647*, 2020. 4

[77] H. Sun, C. Li, B. Liu, Z. Liu, M. Wang, H. Zheng, D. D. Feng, and S. Wang, “Aunet: Attention-guided dense-upsampling networks for breast mass segmentation in whole mammograms,” *Physics in Medicine & Biology*, vol. 65, no. 5, p. 055005, 2020. 4

[78] S. Woo, J. Park, J.-Y. Lee, and I. So Kweon, “Cbam: Convolutional block attention module,” in *Eur. Conf. Comput. Vis.*, 2018, pp. 3–19. 5

[79] A. G. Roy, N. Navab, and C. Wachinger, “Recalibrating fully convolutional networks with spatial and channel “squeeze and excitation” blocks,” *IEEE transactions on medical imaging*, vol. 38, no. 2, pp. 540–549, 2018. 5

[80] M. D. Zeiler and R. Fergus, “Visualizing and understanding convolutional networks,” in *Eur. Conf. Comput. Vis.*, 2014, pp. 818–833. 6

[81] K. Xuan, S. Sun, Z. Xue, Q. Wang, and S. Liao, “Learning mri k-space subsampling pattern using progressive weight pruning,” in *International Conference on Medical Image Computing and Computer-Assisted Intervention*. Springer, 2020, pp. 178–187. 6

[82] O. Ronneberger, P. Fischer, and T. Brox, “U-net: Convolutional networks for biomedical image segmentation,” in *International Conference on Medical image computing and computer-assisted intervention*. Springer, 2015, pp. 234–241. 6

[83] S. Wang, H. Cheng, L. Ying, T. Xiao, Z. Ke, H. Zheng, and D. Liang, “Deepcomplexmri: Exploiting deep residual network for fast parallel mr imaging with complex convolution,” *Magnetic Resonance Imaging*, vol. 68, pp. 136–147, 2020. 6

[84] J. Zbontar, F. Knoll, A. Sriram, M. J. Muckley, M. Bruno, A. Defazio, M. Parente, K. J. Geras, J. Katsnelson, H. Chandarana *et al.*, “fastmri: An open dataset and benchmarks for accelerated mri,” *arXiv preprint arXiv:1811.08839*, 2018. 7